Multicomponent and source-free converted-wave reverse-time migration for VSP

Yue Du, Yunyue Elita Li, Jizhong Yang, Arthur Cheng, National University of Singapore and Xinding Fang, Southern University of Science and Technology*

SUMMARY

VSP has advantages to detect and monitor the objects around the borehole due to its geometry. Multicomponent VSP can add rich information about the elastic properties of the subsurface near wellbore. However, the elastic wave imaging has been challenging due to the complexities in wave physics. The uncertainties in near surface structure will also affect the image accuracy. In this abstract we utilize the elastic image conditions with scalar wave equations for VSP reverse-time migration (RTM) to image the complex structures. We also provide an alternative way of using the source-free converted-wave (SFCW) RTM imaging for VSP to avoid the complex overburden structures. With multiple numerical examples, the PP, PS and SFCW images demonstrate the ability to image the complex sediment layers around the wellbore. Using both PP and PS image can provide a good interpretation for the complex subsurface but they rely on a relatively correct velocity model. The SFCW image is target oriented and is robust for the complex overburden velocity issue, while it has a lack of illumination for the areas further away from the borehole.

INTRODUCTION

VSP has been widely recognized as an effective tool for imaging the small target area around the borehole. It has advantages over surface seismic in the fact that the receivers are deployed in the well in depth, thus it is much closer to the objects to be imaged, and have shorter reflection paths. In recent years, RTM has been widely used for VSP to detect steep dips and complex geometries around the borehole (Haldorsen et al., 2015; Shi and Wang, 2015; Xue and Liu, 2017). As a prestack two-way wave equation migration method, RTM honors wave propagation in all directions, which is more accurate for imaging complex structures (McMechan, 1983). With ongoing improvements in multicomponent seismic acquisition and computational capability, elastic converted-wave processing and imaging are adding additional useful informations of the subsurface (O'Brien and Harris, 2006). It can benefit structural and lithological understanding of subsurface with joint interpretation of the conventional P-wave reflection images and the converted PS images.

Li et al. (2018) derives the elastic imaging condition from a new set of two coupled second-order equations for P- and S-potentials, which provides a much more rigorous theoretical basis for the vector-based elastic wave imaging condition (Du et al., 2012; Wang and McMechan, 2015; Wang et al., 2016; Shabelansky et al., 2017; Du et al., 2017). This image condition automatically takes care of the S-wave polarity without the need of any additional correction using propagation angles or the structural dips. And it can be implemented by only using acoustic propagators, which reduces the computational cost and the artifacts in the images. Because the conventional converted-wave RTM imaging need a forward propagation of P-wave source wavefield, it will be affected by the complex overburden velocities. Therefore, an alternative approach of elastic converted-wave imaging is developed by only using recorded receiver data to avoid the complex overburden structures. He et al. (2008) outline the concept of data-referenced-only migration for VSP, which only use the back projected receiver wavefields. Xiao and Schuster (2009) and Xiao and Leaney (2010) apply this concept to VSP data using PP- and PS-transmissions to image the salt flank. Shabelansky et al. (2014, 2017) summarize this type of seismic imaging condition as source-independent converted-wave imaging condition (SICW-IC). We derive a similar source-free converted-wave imaging condition (SFCW-IC) based on the coupled P- and S-potential equations and point out that the SFCW image is highly dependent on the source spacing (Du et al., 2018). The images obtained from the SFCW imaging condition are second-order approximations to the shear modulus perturbations and can kinematically image the reflectors with large contrast.

In this abstract, we verify the PP, PS and SFCW imaging conditions for VSP geometry and apply them on a simple dip layer model and the complex SEAM model. We show that PP and PS images have different illumination areas and combining them can provide a better interpretation for subsurface imaging. We also discuss the applications for VSP SFCW image and show its advantage when the overburden velocity is uncertain.

METHOD

PP and PS image conditions

Li et al. (2018) derives the elastic imaging conditions from a new set of two coupled P- and S-potential equations, which are consistent with the vector-based elastic wave imaging:

$$I_{PP} = 4\left(\nabla^2 P_0\right)(\Pi_p)^{-*}\delta d_p, \tag{1}$$

$$I_{PS} = -2(\nabla P_0)\cdot(\nabla\times(\Pi_s)^{-*}\delta\mathbf{d_s}) \tag{2}$$

where P_0 is the background P-wave fields, δd_p and $\delta\mathbf{d_s}$ are the perturbed P- and S-wave data residuals. In these equations, $\Pi_p = \frac{\partial^2}{\partial t^2} - \alpha_0\nabla^2$ and $\Pi_s = \frac{\partial^2}{\partial t^2} - \beta_0\nabla^2$ are noted as the propagation operators for P- and S-waves, respectively. $(\Pi_p)^{-*}\delta d_p$ and $(\Pi_s)^{-*}\delta\mathbf{d_s}$ indicate the adjoint P- and S-wave fields which backward propagate the P- and S-wave data residuals with P- and S-wave background velocities.

SFCW image condition

We derive the SFCW image condition based on the same coupled equations and use the back propagated P- and S-receiver

wavefields:

$$I_{SFCW} = -2\nabla(\Pi_p)^{-*}\delta d_p \cdot \nabla \times (\Pi_s)^{-*}\delta \mathbf{d_s} \qquad (3)$$

These image conditions can be efficiently implemented using acoustic propagators for separated P- and S-waves.

IMAGING RESULTS AND DISCUSSIONS

Simple model

We first verify the image conditions on a simple dip layer model (Figure 1a), which have one flat layer on the top and three dipping layers on the bottom. We model the elastic data by solving the first-order elastic wave equations with a staggered-grid implementation of finite difference (Fang et al., 2013). The time step is 0.5 ms, and the grid spacing is 5 m in both x- and z-directions. There are 51 sources spreading along the surface evenly with 30 m shot spacing. The sources are explosive sources with a 20 Hz Ricker wavelet. An array of receivers (black line) is placed along the well trajectory at $x = 0$ m from 400 to 1200 m depth.

Figure 2 shows the PP, PS and SFCW images obtained by the proposed image conditions using acoustic propagator, respectively. They demonstrate that the proposed image conditions are suitable for VSP. Comparing Figure 2a and b, we can observe that the PP image can illuminate further from the well while the PS image has a higher resolution. The migration smiles in PS image are closer to the well and the far-offset image is formed by the transmitted waves. The SFCW image shows similar result with the conventional PS image but have lower resolution due to limited angle coverage between reflected P- and S-waves (Du et al., 2018).

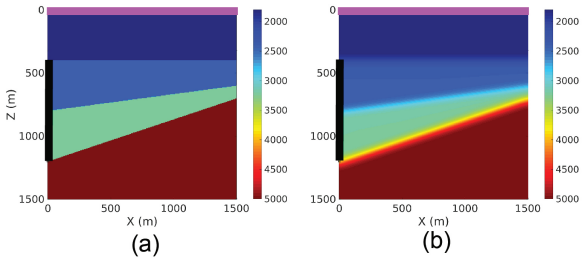

Figure 1: (a) A simple dip layer model. (b) The smoothed dip layer model. The purple line are sources on the surface and the black line indicates the receiver array. We use a constant density model ($\rho = 2500$ kg/m^3) and a constant $V_p/V_s = 1.73$..

The SFCW has advantage that it only requires local velocity model. For example, when the source location is uncertain or the overburden velocity is complex, the conventional PP and PS image will be distorted by the wrong propagation path from the surface sources to vertical receivers. However, the SFCW image can still be used to detect the large contrast around the wellbore. Figure 3 shows the PP, PS and SFCW images that migrated with a wrong velocity model, which changes the first flat layer velocity from 1800 m/s to 1200 m/s. The events in PP and PS images are pulled up by the slower migration velocity but the events in SFCW image are still reliable.

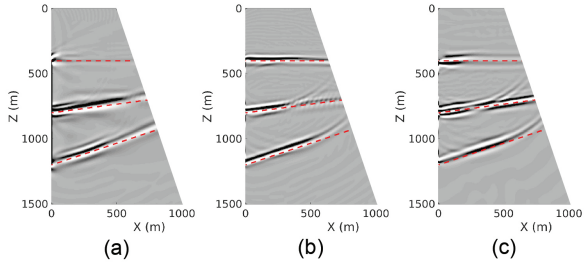

Figure 2: (a), (b) and (c) are the PP, PS and SFCW images migrated with the smoothed dip layer model, respectively. The red dash line indicates the true reflector positions.

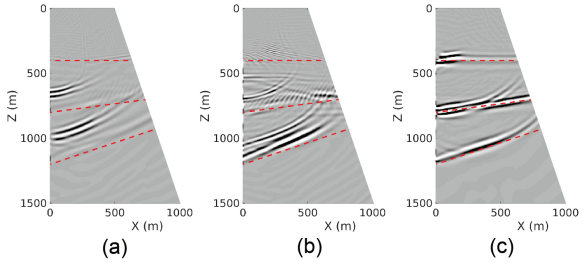

Figure 3: (a), (b) and (c) are the PP, PS and SFCW images migrated with the wrong shallow layer velocity model, respectively.

SEAM model

In this section, we utilize the elastic image conditions on the SEAM model, which is a realistic and complex representation of a typical Gulf of Mexico salt structure. The 3D SEAM model measures 35 km east-west by 40 km north-south by 15 km depth (Fehler and Keliher, 2011). In this study, we use a modified 2D-slice of the SEAM model (Figure 4) in the east-west direction at north 23900 m. The model dimensions are 4 km in both x and z directions. Sources (purple line) spread along the surface from 0 to 2100 m with 30 m shot spacing. An array of receivers (black line) is placed along the well trajectory at $x = 0$ m from 300 to 3000 m depth. We model the VSP data by elastic propagator and separate them to P- and S-wave potential data using Helmholtz decomposition. The grid spacing is 5m in both x and z, and the time step is 0.5 ms. The source wavelet is a Ricker wavelet with a 20 Hz center frequency. Figure 5 shows the smoothed velocity models for migration which get rid of the salt velocity imprints.

Figure 6 presents the PP, PS and SFCW images migrated with the smoothed sediment flood model in Figure 5. The PP image can reflect both P and S perturbations while the PS and SFCW images are only formed by S perturbations. Both PP and PS images can image the complex salt sediments. PP and PS images have different illumination area for salt sediments due to different reflection angles. PP image can illuminate further from the well while PS image illuminates close to the bore-

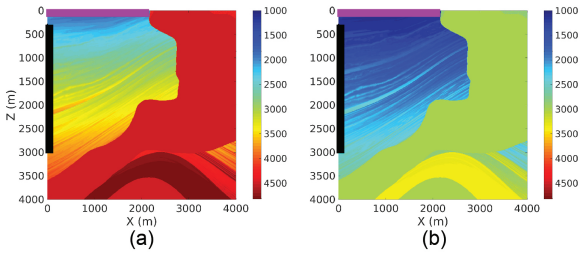

Figure 4: (a) A modified SEAM 2D P and (b) S velocity model. The purple line indicates the sources on the surface and the black line indicates the receiver array. We use a constant density model ($\rho = 2500$ kg/m^3).

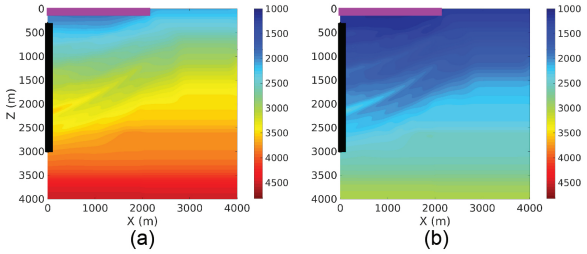

Figure 5: (a) The smoothed sediment flood model of the 2D SEAM model in V_p and (b) V_s for migration.

hole. The PS image has a higher resolution than PP image, and can detect finer sediment layers. However, the PS image is more noisy because it contains higher frequency content. The SFCW image is very similar with the conventional PS image around the borehole where the reflection ray path is short. However, the quality of the SFCW image is degraded with the increasing offset in both vertical and horizontal directions. This is because the energy from the far-offset is weaker and the SFCW image contains strong artifacts due to the crosstalks between different layers. Because P-wave speed is higher than S-wave speed, the nearer PP-events will catch up with the further PS-events and generate severe crosstalk artifacts, thus the image from far-offsets is diminish.

Using the sediment flood model in Figure 5 , both PP and PS image can detect the steep salt flank while the SFCW image cannot image that far. In this study, we do not preprocess the VSP data before migration. The RTM imaging can fully utilize all directions of the waves and do not require an up- and down-wavefield separation as normal VSP process do. And in this case, the reflections from the vertical salt flanks are actually downgoing waves for VSP geometry. Thus it is necessary to back propagate the whole receiver wavefields to detect the vertical salt flanks (pointed by green arrow in Figure 6). The PP image shows a better result of the vertical salt flank, especially for the upper salt boundary. This may due to the badly smoothing of the S-wave velocity model. The PP and PS image can also provide a good image for the dipping salt boundaries (pointed by blue arrow in Figure 6) and even the structures inside the salt (pointed by red arrow in Figure 6). We can notice that the structures inside the salt are at different positions in PS and PP images, which also indicate that the illumination of the PS image is closer to the borehole and the illumination of the PP image is further from the borehole. Thus combining the PP and PS images can provide a better interpretation for the complex structures.

Although the SFCW image cannot detect formations far away from wellbore, it is more suitable for the near wellbore imaging and robust to the complex overburden velocity changes. When the overburden geometry is complex and the near surface velocity model is wrong, the SFCW image can still provide correct information below the overburden structures. In Figure 7, we compare the previous imaging results (top) with the results migrated with a faster shallow layer model (bottom) and zoom in on the shallow portions. The overburden velocity issue have strong impact on the shallow layers and have less impact on the deeper part, thus the change in deeper layers is not as obvious as shallow layers. Figure 7 clear shows that the events in PP and PS images are pushed down by the fast migration velocities while the SFCW image remains the same. The PP and PS images are also degraded by the wrong near surface velocities and the image quality become lower. The SFCW image only requires local velocity model and is robust to the velocity changes in shallow layers or in far-offset formations.

The PP, PS and SFCW images in this study are all constructed by acoustic propagators and free of velocity imprints. This RTM imaging process utilizes the full elastic wavefield without having to do an elastic RTM, which makes it simple and efficient to implement. In future study, we will continue to improve image qualities by reducing migration artifacts through signal processing techniques, as well as investigate other imaging conditions.

CONCLUSIONS

We have verified the elastic imaging conditions for VSP RTM imaging and demonstrate their ability to image the complex geometries. Joint interpretation of the PP and PS image can provide a better understanding for the subsurface structures due to different illuminations. However, when the near surface velocity is inaccurate, structures on PP and PS images are defocused and shifted with respect to their true positions, The SFCW image, on the other hand, remains focused and accurate because it does not need the source-side information. Hence, the SFCW image is robust against the velocity errors that occur around the sources but away from the receivers.

ACKNOWLEDGMENTS

The authors acknowledge the EDB Petroleum Engineering Professorship for financial support. Yunyue Elita Li and Jizhong Yang are funded by MOE Tier-1 Grant R-302-000-165-133. Xinding Fang is supported by National Natural Science Foundation of China (grant 41704112).

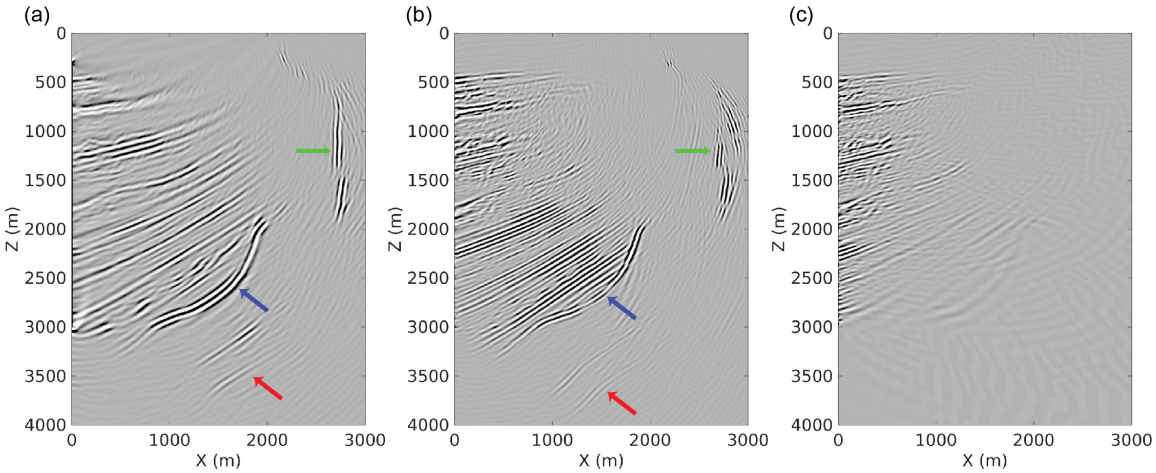

Figure 6: (a), (b) and (c) are the PP, PS and SFCW images migrated with the smoothed velocity model, respectively.

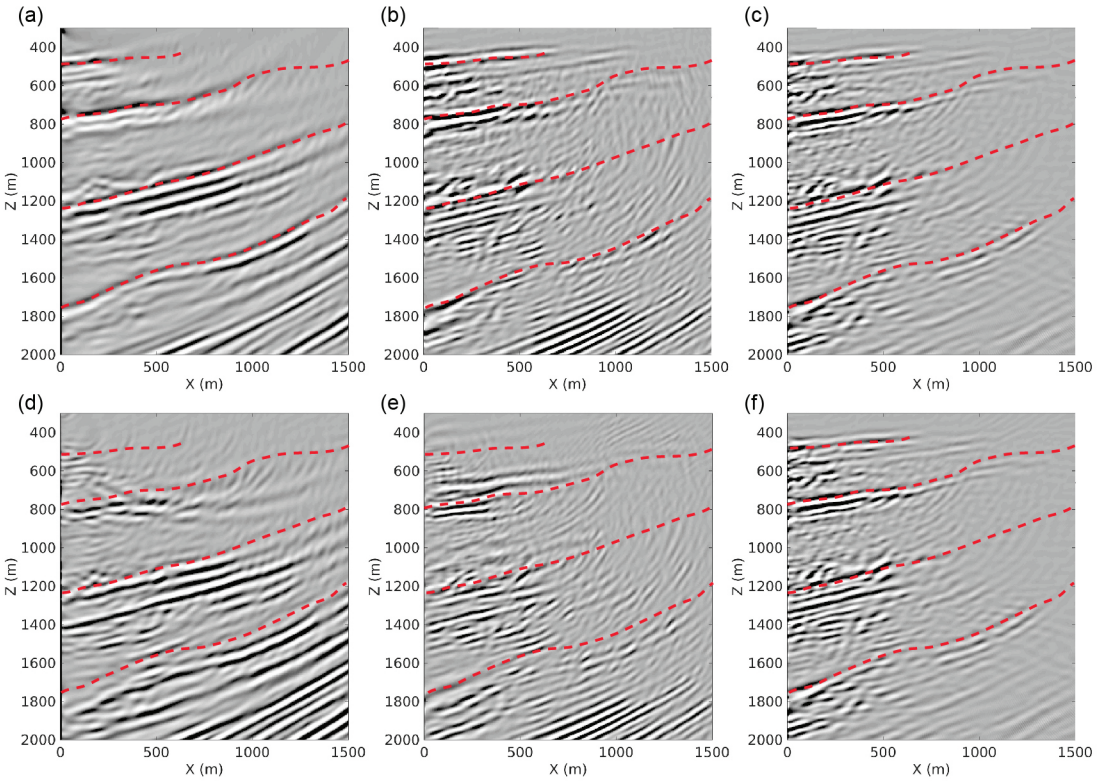

Figure 7: (a), (b) and (c) are the zoomed portion of the PP, PS and SFCW images migrated with the smooth velocity model, respectively. (d), (e) and (f) are the corresponding PP, PS and SFCW images migrated with a wrong overburden velocity model, respectively. The red dash line indicates the reflector positions.

REFERENCES

Du, Q., C. Guo, Q. Zhao, X. Gong, C. Wang, and X. Li, 2017, Vector-based elastic reverse time migration based on scalar imaging condition: Geophysics, **82**, S111–S127.

Du, Q., Y. Zhu, and J. Ba, 2012, Polarity reversal correction for elastic reverse time migration: Geophysics, **77**, S31–S41.

Du, Y., Y. Li, J. Y. Yang, A. Cheng, and X. Fang, 2018, Source-free converted-wave reverse-time migration using acoustic propagators: Beijing 2018 International Geophysical Conference and Exposition, Beijing, China, 24-27 April.

Fang, X., X. Shang, and M. Fehler, 2013, Sensitivity of time-lapse seismic data to fracture compliance in hydraulic fracturing: Geophysical Journal International, **195**, 1843–1861.

Fehler, M. C., and P. J. Keliher, 2011, SEAM Phase I: Challenges of subsalt imaging in tertiary basins, with emphasis on deepwater gulf of mexico.

Haldorsen, J., N. Brooks, P. Donais, W. Heigl, and F. Li, 2015, A migration approach to generating continuous images of salt and sediment boundaries from multi-offset vsp data: 1027–1031.

He, R., M. Karrenbach, and B. Paulsson, 2008, VSP data-referenced-only migration without overburden: 78th Annual International Meeting, SEG, Expanded Abstracts, 3405–3409.

Li, Y., Y. Du, J. Y. Yang, A. Cheng, and X. Fang, 2018, A separated formulation of the elastic wave equation in P- and S-potential fields: 67th Annual EAGE Meeting, EAGE, Expanded Abstracts, 280.

McMechan, G., 1983, Migration by extrapolation of time-dependent boundary values: Geophysical Prospecting, **31**, 413–420.

O'Brien, J., and R. Harris, 2006, Multicomponent vsp imaging of tight-gas sands: Geophysics, **71**, E83–E90.

Shabelansky, A., A. Malcolm, M. Fehler, X. Shang, and W. Rodi, 2014, Source-independent full wavefield converted-phase elastic migration velocity analysis: Geophysical Journal International, **200**, 954–968.

Shabelansky, A. H., A. Malcolm, and M. Fehler, 2017, Converted-wave seismic imaging: Amplitude-balancing source-independent imaging conditions: Geophysics, **82**, S99–S109.

Shi, Y., and Y. Wang, 2015, Reverse time migration of 3D vertical seismic profile data: Geophysics, **81**, S31–S38.

Wang, C., J. Cheng, and B. Arntsen, 2016, Scalar and vector imaging based on wave mode decoupling for elastic reverse time migration in isotropic and transversely isotropic media: Geophysics, **81**, S383–S398.

Wang, W., and G. A. McMechan, 2015, Vector-based elastic reverse time migrationvector-based elastic rtm: Geophysics, **80**, S245–S258.

Xiao, X., and W. S. Leaney, 2010, Local vertical seismic profiling (VSP) elastic reverse-time migration and migration resolution: Salt-flank imaging with transmitted P-to-S waves: Geophysics, **75**, S35–S49.

Xiao, X., and G. T. Schuster, 2009, Local migration with extrapolated VSP greens functions: Geophysics, **74**, SI15–SI26.

Xue, H., and Y. Liu, 2017, VSP reverse time migration based on complex wavefield decomposition: SEG 2017 Workshop: Carbonate Reservoir EP Workshop, Chengdu, China, 22-24 October 2017, 152–155.